AGU PUBLICATIONS

JGR

Journal of Geophysical Research: Oceans

RESEARCH ARTICLE

10.1002/2014JC010439

Key Points:

- Cross-pol radar sea return varies with incidence angle
- Design cross-pol geophysical model function
- Retrieve high wind velocity using cross-pol radar sea returns

Correspondence to:
P. Hwang,
paul.hwang@nrl.navy.mil

Citation:
Hwang, P. A., A. Stoffelen, G.-J. van Zadelhoff, W. Perrie, B. Zhang, H. Li, and H. Shen (2015), Cross-polarization geophysical model function for C-band radar backscattering from the ocean surface and wind speed retrieval, *J. Geophys. Res. Oceans*, *120*, 893–909, doi:10.1002/2014JC010439.

Received 9 SEP 2014
Accepted 12 JAN 2015
Accepted article online 22 JAN 2015
Published online 13 FEB 2015

Cross-polarization geophysical model function for C-band radar backscattering from the ocean surface and wind speed retrieval

Paul A. Hwang[1], Ad Stoffelen[2], Gerd-Jan van Zadelhoff[2], William Perrie[3], Biao Zhang[3,4], Haiyan Li[3,5], and Hui Shen[3,6]

[1]Remote Sensing Division, Naval Research Laboratory, Washington District of Columbia, USA, [2]Royal Netherlands Meteorological Institute, De Bilt, Netherlands, [3]Fisheries and Oceans Canada, Bedford Institute of Oceanography, Dartmouth, Nova Scotia, Canada, [4]School of Marine Sciences, Nanjing University of Information Science and Technology, Nanjing, China, [5]Key Laboratory of Computational Geodynamics, Chinese Academy of Sciences, University of Chinese Academy of Sciences, Beijing, China, [6]Institute of Oceanology, Chinese Academy of Sciences, Qingdao, China

Abstract The wind speed sensitivity of cross-polarization (cross-pol) radar backscattering cross section (*VH*) from the ocean surface increases toward high winds. The signal saturation problem of *VH*, if it exists, occurs at a much higher wind speed compared to the copolarization (copol: *VV* or *HH*) sea returns. These properties make *VH* a better choice over *VV* or *HH* for monitoring severe weather. Combined with high spatial resolution of the synthetic aperture radar (SAR), the development of hurricane wind retrieval using *VH* is advancing rapidly. This paper describes a cross-pol C-band radar backscattering geophysical model function (GMF) with incidence angle dependence for the full wind speed range in the available data sets (up to 56 m/s). The GMF is derived from RADARSAT-2 (R2) dual-polarization (dual-pol) ScanSAR modes with 300 and 500 km swaths. The proposed GMF is compared to other published algorithms. The result shows that the simulated *VH* cross section and the retrieved wind speed with the proposed GMF is in better agreement with measurements. With careful treatment of noise, the *VH*-retrieved wind speeds may extend to mild or moderate conditions. The higher fraction of non-Bragg contribution in *VH* can be exploited for analysis of surface wave breaking.

1. Introduction

Recent studies reveal that the cross-pol radar backscattering from the ocean surface has the property of increasing sensitivity toward high winds and signal saturation, if exists, delayed to much higher wind speeds compared to copol returns. These attributes make *VH* a desirable remote-sensing parameter for monitoring severe weather [*Hwang et al*., 2010a, 2010b; *Zhang et al*., 2011; *Vachon and Wolfe*, 2011]. (Here we use *VH* for either σ_{0VH} or σ_{0HV}: normalized radar cross section of vertical transmit horizontal receive or horizontal transmit vertical receive.) Efforts to explore hurricane wind retrieval using *VH* from polarimetric SAR imagery were developed concurrently [e.g., *Zhang et al*., 2011, 2012, 2014; *Zhang and Perrie*, 2012; *Horstmann et al*., 2013; *van Zadelhoff et al*., 2013, 2014]. There is also consideration of incorporating *VH* channel in the next generation scatterometer designs [*Lin et al*., 2012; *Belmonte Rivas et al*., 2014]. The *VH* signal can improve the wind direction resolution for the *VV* measurement since it adds information on the absolute wind speed, thus improving the retrieval of the remaining unknown wind direction. It may improve coastal wind retrieval since the *VH* does not require overlap of three beams but a single measurement to obtain absolute wind speed. There are also indications that the fraction of breaking contribution for the *VH* sea return is higher in comparison to copol returns. This property is useful for breaking wave research [e.g., *Hwang et al*., 2010a, 2010b; *Fois et al*., 2014].

So far, the algorithms for hurricane wind retrieval or scatterometer design simulations using GMFs assume that *VH* varies mainly with wind speed (U_{10}) and is independent on the azimuth angle (ϕ). Its dependence on the incidence angle (θ) is either absent [*Zhang et al*., 2011, 2012, 2014; *Zhang and Perrie*, 2012; *Belmonte Rivas et al*., 2014] or is noted only in the low-to-strong wind speed range ($U_{10} < 21$ m/s) in the GMF established with the European Center for Medium-range Weather Forecast (ECMWF) winds [*van Zadelhoff et al*., 2013, 2014]. For the range of incidence angles typical of the polarimetric SAR imagery used in hurricane wind retrieval and METOP (Meteorological Operational) second-generation scatterometer design (about 20°–50°), the difference in the *VH* cross section is equivalent to about ±5 m/s retrieved wind speed. The azimuth dependence is examined in *van Zadelhoff et al*. [2013, 2014], but no wind direction dependence can be determined, which is in great contrast to the copol (*VV*) measurements. They conclude that any *VH* dependence on azimuth angle is small in comparison to the wind speed dependence. For low-to-strong wind speeds (U_{10} up to ~24 m/s), analyses of field data yield results of azimuthal variations of Ku, C, and L-band *VH* backscattering ranging from comparable to, to about one half of the copol azimuthal variations [*Yueh et al*., 2002, 2010; *Zhang et al*., 2012; *Hwang et al*., 2014]. The clarification of azimuthal variation is of great interest with regard to the surface roughness and wave breaking properties. Both copol and cross-pol microwave backscattering are expected to exhibit azimuthal variation following the theoretical consideration of Bragg scattering from the ocean surface roughness [e.g., *Valenzuela*, 1967; *Hwang et al*., 2010b; *Voronovich and Zavorotny*, 2011, 2014]. The observation of *VH* azimuthal variation can assist in clarifying the directional distribution of surface wave breaking causing the non-Bragg contribution.

In a reanalysis of the data set used in *Zhang et al*. [2014] combining collocated dual-pol C-band R2 SAR polarimetric returns with buoy, stepped frequency microwave radiometer (SFMR) and H*Wind data sources, *Hwang et al*. [2014] conclude that the range of *VH* variation with incidence angle is consistent with theoretical expectations [e.g., *Valenzuela*, 1967; *Hwang et al*., 2010b; *Voronovich and Zavorotny*, 2011, 2014] over the full range of wind speeds available in the data set (up to 38 m/s). Although the magnitude of *VH* drop is much smaller (2–3 dB between 20° and 50° incidence angle) in the high wind region ($U_{10} > \sim 20$ m/s) compared to that in lower winds, the rate of wind speed change per dB is much larger (4–5 m/s per dB); thus, the difference in the *VH* cross section in strong-to-severe winds (>~20 m/s) is also equivalent to about ±5 m/s retrieved wind speed. The incidence angle dependence remains strong in numerical simulations incorporating breaking wave considerations [*Fois et al*., 2014]. It is therefore important to establish a *VH* GMF with the incidence angle factored in for the full range of wind speeds.

To develop an accurate GMF, several requirements should ideally be met in order to obtain an accurate estimate [e.g., *Stoffelen and Anderson*, 1997a, 1997b]:

1. Uniform quality input data, or, at least, input data with known error properties.
2. Tailor-made numerical estimation of the GMF in case the measurement errors of the inputs depend on the measured values or in case the GMF is nonlinear.
3. Well-sampled input data.

Given the limited coverage of relevant parameters in the available data (to be described in section 2.1), these requirements are not met here. In particular, the input reference neutral wind velocity at 10 m elevation (U_{10}) originates from diverse sources. The different spatial and temporal collocation criteria and different data manipulation of the data sources are particularly problematic in representing the extremes of the speed distribution. Artificial decorrelation and apparent saturation may also result from horizontal smearing [e.g., *Stoffelen*, 1998]. For example, local hurricane winds are gusty and a gust measured by SFMR may not be detected by R2 or the ECMWF model.

Moreover, SFMR data appear contaminated by heavy rain [*Klotz and Uhlhorn*, 2012], H*Wind product is not direct measurements of U_{10} [*DiNapoli et al*., 2012], and ECMWF winds are from a rather coarse numerical weather prediction (NWP) model. These limitations cannot be avoided and, therefore, the statistical results in this study should be evaluated with caution. Nevertheless, the need to have a *VH* GMF reflecting more realistically the incidence angle dependence is urgent, as the development of *VH* applications is proceeding rapidly.

Making use of the analysis results derived from *Hwang et al*. [2014], here we present a cross-pol C-band GMF suitable for R2 dual-pol wide swath data. The formulation is described in section 2, and comparisons with other cross-pol GMFs [*van Zadelhoff et al*., 2013, 2014; *Zhang et al*., 2014] are presented in section 3. The applications to *VH* simulation and wind speed retrieval are evaluated in section 4. A particular issue of employing the cross-pol returns is their low signal-to-noise ratio (SNR), especially in low winds (where the incidence angle variation is strongest) and at high incidence angles. Because an earlier data set used in the present analysis did not extract the noise information of backscattering measurements, the data processing

Table 1. Some Basic Statistics of the Data Sets Used in This Study

θ	N	U_{10min}	U_{10max}	N_1	N_2	N_3	N_4	N_5
a. BSH								
20–25	237	4.16	26.40	86	79	72	0	0
25–30	351	3.73	28.77	143	100	108	0	0
30–35	538	3.73	35.08	178	126	207	27	0
35–40	439	3.73	37.97	118	151	114	56	0
40–45	182	4.00	27.00	48	93	41	0	0
45–50	76	6.38	16.00	50	26	0	0	0
All	1845	3.73	37.97	626	586	550	83	0
$VH > -28$ dB	1564	3.73	37.97	382	549	550	83	0
b. KNMIS								
20–25	4853	7.70	29.40	21	2043	2789	0	0
25–30	7225	1.80	33.60	127	1626	4511	961	0
30–35	10,982	6.70	43.80	45	3242	4599	2939	157
35–40	11,913	2.00	43.30	523	3217	5058	2884	231
40–45	9695	1.00	56.00	240	1748	3810	3013	884
45–50	5775	2.80	44.90	376	817	3710	782	90
All	50,644	1.00	56.00	1332	12,763	24,608	10,579	1362
$VH >$ NESZ + 1 dB	49,509	1.00	56.00	782	12,179	24,607	10,579	1362
c. KNMIE								
20–25	62,511	0.24	29.15	19,028	40,051	3432	0	0
25–30	66,031	0.89	27.22	14,273	45,545	6213	0	0
30–35	71,431	0.91	32.43	11,241	49,292	10,758	140	0
35–40	76,362	0.73	37.63	10,572	49,478	15,585	727	0
40–45	76,660	0.10	37.57	16,641	45,785	12,048	2186	0
45–50	73,495	3.33	35.02	25,394	35,505	12,064	532	0
All	432,879	0.09	37.63	99,755	269,339	60,200	3585	0
$VH >$ NESZ + 1 dB	374,781	0.09	37.63	49,967	261,081	60,148	3585	0

to recover the weak signals becomes an important consideration. The description of noise treatment is given in section 5, with additional discussions on the retrieval wind speed range using *VH* and the extension of *VH* application to surface wave breaking investigation. Finally, a summary is given in section 6.

2. VH GMF

2.1. Data Sets and General Properties of VH

In order to obtain a better coverage in wind speed U_{10} and incidence angle θ, three data sets of R2 dual-pol (*VV* and *VH*) wide swath radar backscattering and collocated wind velocity from various sources are combined in this study: (1) BSH, with wind data from Buoy, SFMR, and H*Wind sources [*Zhang et al.*, 2014]; (2) $KNMI_S$, with wind data from SFMR measurements assembled at the Royal Netherlands Meteorological Institute (KNMI) [*van Zadelhoff et al.*, 2013, 2014]; and (3) $KNMI_E$, with wind data from ECMWF simulations [*van Zadelhoff et al.*, 2013, 2014]. Significantly, the two KNMI data sets are collected under 19 hurricane scenes and the noise-equivalent sigma-zero (NESZ) data are extracted. The SFMR and H*Wind portion of the BSH data set is also under hurricane wind conditions, but the NESZ is not extracted in the BSH data set.

Table 1 lists some of the basic properties of the three data sets: the number of data points *N*, minimal wind speed U_{10min}, maximum wind speed U_{10max}, and the numbers of data points in wind speed ranges 0–10, 10–20, 20–30, 30–40, and 40+ m/s, respectively, N_1, N_2 N_3, N_4, and N_5. The statistics are listed for each 5° θ bin between 20° and 50°.

As mentioned in section 1, the *VH* dependence on θ and ϕ has been analyzed using the BSH data set [*Hwang et al.*, 2014]. Figure 1 plots the average σ_{0VH} as a function of wind speed sorted in six θ bins. The SNR of *VH* is low, especially in dual-pol configuration, the σ_{0VH} shown in Figure 1a has the nominal noise floor of 10^{-3} or -30 dB subtracted [*Hwang et al.*, 2010a]. *Hwang et al.* [2014] summarize the *VH* dependence on incidence angle as following: the *VH* data can be roughly divided into three wind speed groups: WSG1 ($U_{10} < \sim 15$ m/s), WSG2 (U_{10} between $\sim$15 and 30 m/s), and WSG3 ($U_{10} > \sim 30$ m/s). Consistent with previous findings [*Hwang et al.*, 2010a, 2010b], the wind sensitivity of *VH* increases toward high winds: approximately linearly for WSG1 and quadratically for WSG2. However, the expanded data set in the present collection suggests that the increasing sensitivity may not extend beyond about 30 m/s wind speed.

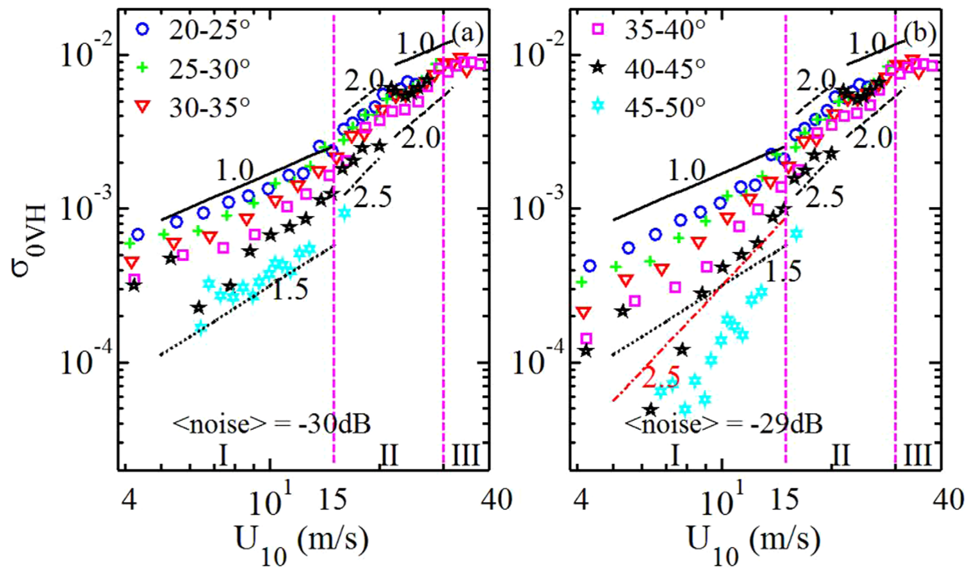

Figure 1. (a) The piecewise power law *VH* dependence on wind speed in three wind speed groups as discussed in *Hwang et al.* [2014]. The mean noise of the BSH data set is assumed to be −30 dB. (b) The same data processed with assumed mean noise of −29 dB.

The decreasing trend of *VH* with increasing θ is quite evident for WSG1. For θ between 20° and 50°, the *VH* has a drop of about 5 dB and it varies with U_{10} at a rate of about 1 dB per 2 m/s. The decreasing trend is less obvious for WSG2, mainly because of limited data coverage (Table 1a). For the available data, the magnitude of *VH* variation with θ is in good agreement with theoretical computation, which shows drops of 3 and 2 dB (θ between 20° and 50°) for wind speeds at 20 and 40 m/s, respectively. The rate of change for $U_{10} > \sim 20$ m/s is about 4–5 m/s per dB increase in *VH*. In WSG3, *VH* becomes nonmonotonic as a function of wind speed, with *VH* leveling off or decreasing as U_{10} exceeds about 30–35 m/s for $\theta = 30°$–40°. However, the U_{10} data from SFMR may be inaccurate as discussed in section 1 and rain information is not in the data set, so whether signal saturation actually occurs remains unclear. For other θ bins, the data coverage is insufficient (Table 1a) to address the signal saturation issue.

During the course of this investigation, we have examined the noise properties of R2 dual-pol (*VV* and *VH*) ocean surface backscattering data in ScanSAR modes (300 and 500 km swaths), using the NESZ included in the KNMI data sets [*van Zadelhoff et al.*, 2013, 2014]. The average noise level is about −29 dB for R2 dual-pol sea returns. Using this noise level to reprocess the BSH data set, the wind speed dependence in the low wind region is significantly modified (Figure 1b). In this paper, −29 dB is used as the mean NESZ for analyzing the BSH data set. More discussion on the *VH* noise and the recovery of weak signal in the absence of noise data is given in section 5 (Note: the NESZ for the wide swath mode listed in Table 2.9 of the R2 product description [*Slade*, 2009] is -28.5 ± 2.5 dB, which is apparently for global average. Our analysis using the ocean data as presented in section 5.1 is somewhat lower.)

2.2. Design of the VH GMF

The proposed GMF is designed by representing the *VH* as piecewise power law functions of wind speed, with the proportionality coefficient and the exponent of the power law function varying with incidence angle and wind speed. Because of the significant differences among different data sets in terms of the data size and coverage in relevant parameters such as wind speed, wind direction, azimuth direction, and radar incidence angle, easy modification of the GMF is an important consideration in order to adapt to better information in the future. For example, the number of WSGs and the parameterization in each WSG can be revised without major changes in the design structure as the database expands and knowledge of the wind speed dependence in each WSG and θ bin becomes more refined.

Basically, the *VH* is expressed as a simple power law function of U_{10} in each WSG for a given θ; that is, for the *n*th WSG, the cross-pol cross section is represented by

$$[\sigma_{0VH}(\theta)]_n = A_n(\theta)U_{10}^{a_n(\theta)}. \tag{1}$$

Ideally, the coefficient A_n and exponent a_n can be derived from field data. Presently, only partial information is available or can be estimated due to a lack of comprehensive coverage in θ and U_{10} in our collected data sets. Some of the parameters can be computed with the requirement of continuity between different WSGs of a given θ. In particular, if only the exponents a_n for all WSGs and a limited number of A_n can be specified, the remaining proportionality coefficients A_n can be obtained by matching the σ_{0VH} of neighboring WSGs at the corresponding transition wind speed U_t. This leads to a recursive equation

$$A_n(\theta) = A_{n-1}(\theta)U_{t(n-1)}^{a_{n-1}(\theta)-a_n(\theta)}, \tag{2}$$

where $U_{t(n-1)}$ is the transition velocity between $(n-1)$th and nth WSGs.

The signal of incidence angle variation is the strongest in the lowest wind speed group (WSG1). This is good because the median wind speed of global wind speed distribution is between 7 and 8 m/s, we can expect to have the most abundant observations in WSG1 for producing A_1 and a_1 in all θ bins. It becomes clear that only a reasonable knowledge of the wind speed exponents in higher wind speed groups is needed for completing the *VH* GMF formulation. The procedure is summarized in the following steps:

Step 1: Divide data into some finite number of θ bins.

Step 2: For each ith θ bin determine the number of WSGs and estimate the appropriate $a_1(\theta_i)$, $U_{t1}(\theta_i)$, $a_2(\theta_i)$, $U_{t2}(\theta_i)$, $a_3(\theta_i)$, $U_{t3}(\theta_i)$, $a_4(\theta_i)$, etc.

Step 3: Use polynomial data fitting and obtain $A_1(\theta_i)$ for each ith θ bin in WSG1.

Step 4: Compute $A_2(\theta_i)$, $A_3(\theta_i)$, etc. using (2).

Step 5: Interpolate $A_n(\theta)$ and $a_n(\theta)$ using the corresponding bin values $A_n(\theta_i)$ and $a_n(\theta_i)$.

Step 6: Compute $\sigma_{0VH}(\theta; U_{10})$ with (1) using the $A_n(\theta)$ and $a_n(\theta)$ determined in steps 1–5.

2.3. VH GMF Parameters

Figure 2 shows $\sigma_{0VH}(U_{10})$ for the three data sets outlined in section 2.1. The various plotting symbols represent data sorted into six θ bins between 20° and 50° with 5° bin width. From visual inspection, BSH and $KNMI_S$ share many similar features (Figures 2a and 2b). These two data sets are used together to formulate the GMF. It is judged that dividing the wind speed range into five or less WSGs can provide a good description of the data in each 5° θ bin. The corresponding parameters a_n and U_{tn} of various WSGs and θ bins are estimated using the two data sets. Finally, the $A_1(\theta_i)$ for each ith θ bin is obtained from least squares fitting using the BSH data in WSG1 because BSH has the best coverage in this low wind group. The resulting $A_1(\theta_i)$, $a_n(\theta_i)$, and $U_{tn}(\theta_i)$ are listed in Table 2a. To serve as a lookup table (LUT) for θ interpolation over the range between 20° and 50°, two additional entries are added for θ bins 15°–20° and 50°–55° by extrapolation. Following the steps outlined in the last section, the computed *VH* curves for the corresponding six θ bins are shown with continuous curves in Figures 2a and 2b.

The $KNMI_E$ data set differs substantially from BSH and $KNMI_S$, resulting in obvious deviations of the *VH* curves from the data (Figure 2c). In particular, the model gives a much lower *VH* for the two high θ bins (42.5° ± 2.5° and 47.5° ± 2.5°), and the trend of data saturation in BSH and $KNMI_S$ data sets (near 30–35 m/s of 32.5° ± 2.5°, 37.5° ± 2.5°, and 42.5° ± 2.5° bins) does not appear in the $KNMI_E$ data set. Adjustments for these differences in $A_1(\theta_i)$, $U_{tn}(\theta_i)$, and $a_n(\theta_i)$ are listed in Table 2b. The calculated *VH* with the adjusted parameters improves agreement with data (Figure 2d). To distinguish between the two variations of the proposed *VH* GMF, subscripts S and E are appended, i.e., GMF_S and GMF_E; the former is applicable to the BSH and $KNMI_S$ data sets and the latter to the $KNMI_E$ data set. This exercise demonstrates the ease of modification for the present GMF design.

The ECMWF data set is based on numerical simulations. The size is considerably larger (400,000+ points) but with coarse spatial and temporal resolutions (0.25° or about 25 km grids, 3 h time steps). The BSH and SFMR data sets have better spatial and temporal differences but suffer from the sampling error due to the small data size.

10.1002/2014JC010439

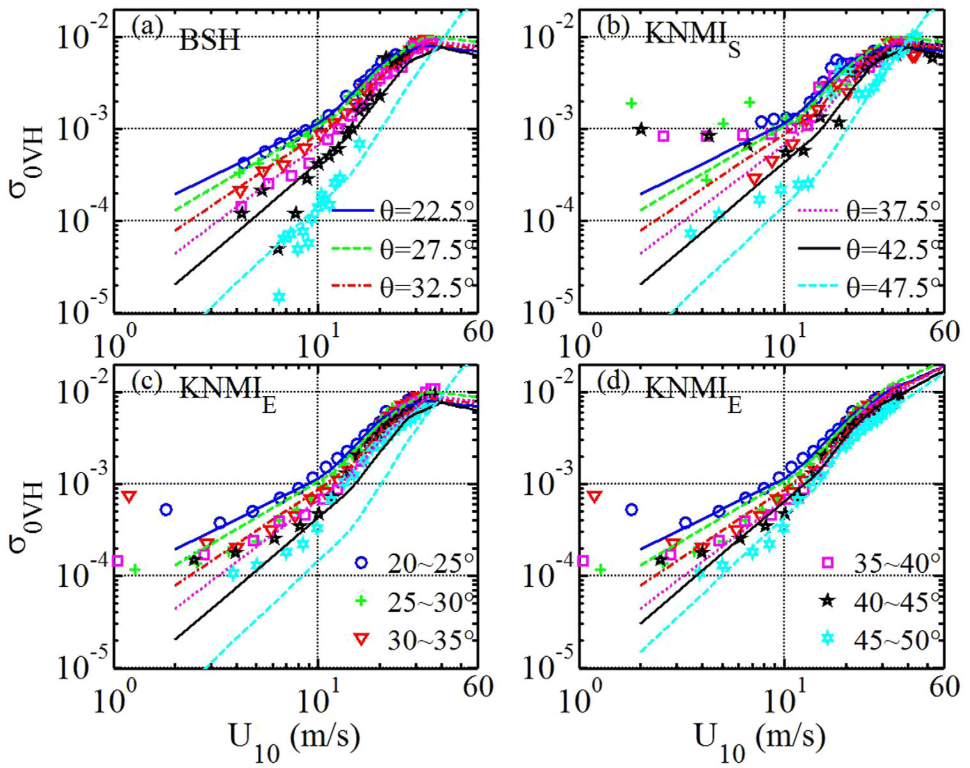

Figure 2. The proposed GMFs applied to three data sets: (a) H14$_S$ for BSH, (b) H14$_S$ for KNMI$_S$, (c) H14$_S$ for KNMI$_E$, and (d) H14$_E$ for KNMI$_E$.

3. Comparison With Other GMFs and Wind Speed Inversion

3.1. VH GMF

Figure 3 shows a comparison of the proposed GMF with three recently reported *VH* GMFs, referred to as vZ13$_S$, vZ13$_E$ [*van Zadelhoff et al*., 2013, 2014], and Z14 [*Zhang et al*., 2014]. In the same convention, the GMFs described in section 3 are called H14$_S$ and H14$_E$. To reduce clutter, we only show data in three θ bins: 22.5° ± 2.5°, 37.5° ± 2.5°, and 47.5° ± 2.5°. The BSH (dark symbols) and KNMI$_S$ (light symbols) data are combined in Figure 3a and the KNMI$_E$ data are shown in Figure 3b.

Table 2. *VH* GMF Parameters

θ	A_1	a_1	U_{t1}	a_2	U_{t2}	a_3	U_{t3}	a_4	U_{t4}	a_5
a. BSH and KNMI$_S$										
17.5	1.40E-04	0.90	10.00	2.00	21.00	1.10	25.00	0.75	30.00	−0.25
22.5	9.06E-05	1.10	11.00	2.25	21.00	1.10	25.00	0.75	33.00	−0.25
27.5	5.33E-05	1.30	12.00	2.35	21.00	1.50	32.00	0.75	35.00	−0.25
32.5	2.79E-05	1.50	14.00	2.50	21.00	1.50	34.00	1.00	35.00	−0.25
37.5	1.34E-05	1.70	15.00	2.70	21.00	2.00	34.00	1.50	35.00	−0.25
42.5	5.44E-06	1.90	15.00	3.00	21.00	2.60	28.00	1.00	40.00	−0.50
47.5	1.15E-06	2.10	15.00	3.60	21.00	3.50	28.00	3.00	50.00	1.50
52.5	8.00E-07	2.30	15.00	3.60	21.00	3.50	28.00	3.00	50.00	1.50
b. KNMI$_E$										
17.5	1.40E-04	0.90	10.00	2.00	21.00	1.50	28.00	0.75	30.00	0.75
22.5	9.06E-05	1.10	11.00	2.25	21.00	1.50	32.00	1.00	33.00	1.00
27.5	5.33E-05	1.30	12.00	2.35	21.00	2.00	32.00	1.00	40.00	1.00
32.5	2.79E-05	1.50	14.00	2.50	21.00	2.00	34.00	1.00	40.00	1.00
37.5	1.34E-05	1.70	15.00	3.00	21.00	2.00	34.00	1.20	40.00	1.20
42.5	8.16E-06	1.90	15.00	3.00	21.00	2.00	28.00	1.20	40.00	1.20
47.5	3.45E-06	2.10	15.00	3.50	21.00	1.50	28.00	1.50	50.00	1.50
52.5	8.00E-07	2.30	15.00	3.20	21.00	1.50	28.00	1.50	50.00	1.50

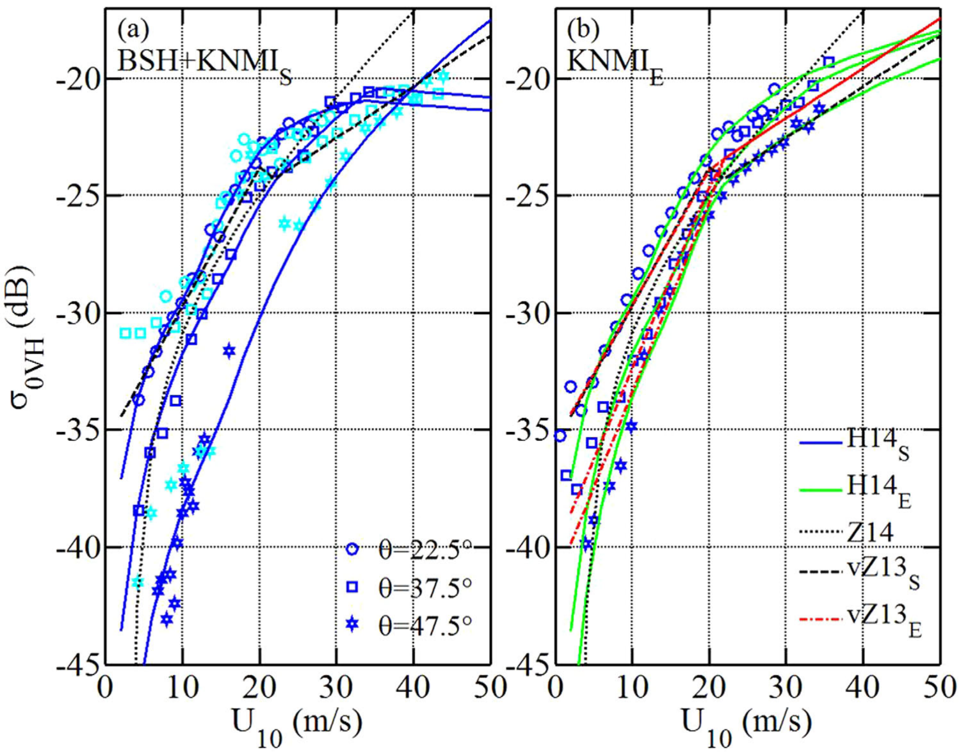

Figure 3. Comparison of various GMFs and data sets: (a) combined BSH (dark symbols) and KNMI$_S$ (light symbols) data sets and H14$_S$, Z14, and vZ13$_S$ GMFs; (b) KNMI$_E$ data set and H14$_E$, Z14, vZ13$_S$, and vZ13$_E$ GMFs.

The Z14 algorithm is derived from fitting a linear function of wind speed to the dual-pol *VH* in dB

$$\sigma_{0VHm}^{dB}=0.332U_{10}-30.143, \tag{3}$$

where σ_{0VHm} is the measured *VH* without removing noise. As discussed in section 2.1, and to be further elaborated in section 5, the mean noise of the dual-pol *VH* is estimated to be -29 dB (i.e., $10^{-2.9}$) so for Z14 $\sigma_{0VH}=\sigma_{0VHm}-10^{-2.9}$ is plotted in Figure 3.

The vZ13$_S$ is established with noise-subtracted R2 *VH* data and collocated SFMR wind speed measurements. It is also given in terms of *VH* in dB as a linear function of U_{10} but in two branches:

$$\sigma_{0VH}^{dB}=\begin{cases}0.592U_{10}-35.60, U_{10}\le 21\mathrm{m/s}\\ 0.218U_{10}-29.07, U_{10}>21\mathrm{m/s}\end{cases}. \tag{4}$$

The vZ13$_E$ is established with noise-subtracted R2 *VH* data and collocated model forecast winds from short-range ECMWF numerical weather prediction:

$$\begin{cases}\sigma_{0VH35}^{dB}=0.76U_{10}-39.53, U_{10}\le 21\mathrm{m/s}\\ \sigma_{0VH}^{dB}=0.213U_{10}-28.09, U_{10}>21\mathrm{m/s}\end{cases}. \tag{5}$$

The *VH* in the low-to-strong wind speed branch of vZ13$_E$ is dependent on incidence angle as discussed in *van Zadelhoff et al*. [2013, 2014, section 2.4.1]. The θ-dependence is formulated as a *VH* deficit, which is defined as the difference between *VH* at a given θ and 35°; the latter reference is expressed as σ_{0VH35} in (5).

Notably, the vZ13$_S$, vZ13$_E$, and Z14 GMFs lack the θ dependence in the high-to-severe wind speed region ($U_{10}>21$ m/s), and all three show significant divergence from each other. This is caused mainly by the difference in the fitting data sets. The Z14 is based on the BSH data set. As shown in Table 1a, the range of θ in the BSH data set with $U_{10}>30$ m/s is restricted to θ between 30° and 40°. In comparison, the KNMI$_S$ and KNMI$_E$ data sets have good coverage of θ higher than 40°, but there are insufficient data for the full θ range to derive an incidence angle dependence for $U_{10}>21$ m/s (Tables 1b and 1c). On the other hand, the divergence between $vZ13_S$ and $vZ13_E$ in high winds is caused by the large difference between the spatial resolution between SFMR and ECMWF products and perhaps by the uncorrected SFMR rain sensitivity, though note that the two KNMI GMFs are only about 1 dB different. More quantitative results of the *VH* simulation and wind speed inversion using these GMFs ($H14_S$, $H14_E$, Z14, $vZ13_S$, and $vZ13_E$) are presented in section 4.

3.2. Wind Speed Retrieval

The algorithm for wind speed inversion using Z14 or $vZ13_S$ is straightforward. With (3),

$$U_{10Z14}=\frac{\sigma_{0VHm}^{dB}+30.143}{0.332}, \tag{6}$$

and with (4),

$$U_{10vZ13S}=\begin{cases}\dfrac{\sigma_{0VH}^{dB}+35.60}{0.592}, \sigma_{0VH}\leq\sigma_{0VHt}\\ \dfrac{\sigma_{0VH}^{dB}+29.07}{0.218}, \sigma_{0VH}>\sigma_{0VHt}\end{cases}. \tag{7}$$

The transition wind speed $U_t=17.46$ m/s is used here to maintain continuity, and the transition *VH* is computed to be $\sigma_{0VHt}=-25.264$ dB.

For the $vZ13_E$ GMF, we use the LUT approach similar to the copol GMF wind retrieval algorithms. For example, at the European Organization for the Exploitation of Meteorological Satellites (EUMETSAT) Ocean and Sea Ice Satellite Application Facility (OSI SAF), the normalized radar cross section (NRCS) is precalculated with the GMF (e.g., CMOD5) for wind speeds from 1 to 60 m/s in 0.2 m/s bins, incidence angles from 15 to 69° in 1° bins, and relative wind directions in 2.5° bins. The backscatter is linearly interpolated to the correct incidence angle but no interpolation is done for wind speed and wind direction, so the resolution of the OSI SAF wind products is 0.2 m/s in wind speed and 2.5° in wind direction [*Hersbach*, 2003; *Verhoef and Stoffelen*, 2013]. The same design is adopted for the $vZ13_E$ wind speed retrieval.

The H14 does not use *VH* in dB unit as the convention of vZ13 and Z14. Instead, the *VH* NRCS in linear units is expressed as a power law function of U_{10} (1), so the algorithm for inversion is also relatively simple:

$$U_{10H14}=\left[\frac{\sigma_{0VH}(\theta)}{A_n(\theta)}\right]^{1/a_n(\theta)}, \tag{8}$$

where subscript *n* denotes the *n*th WSG. The transition *VH* can be written as

$$[\sigma_{0VHt}(\theta)]_{n-1}=A_{n-1}(\theta)U_{t(n-1)}^{a_{n-1}(\theta)}. \tag{9}$$

To avoid the double-value problem in the case of possible signal saturation, for the wind inversion algorithm, the H14 GMF employs only the first 4 WSGs listed in Table 2 (with the high wind limit of WSG4 expanded). Thus, there are three transition wind velocities U_{t1}, U_{t2}, and U_{t3}, with corresponding σ_{0VHt1}, σ_{0VHt2}, and σ_{0VHt3}. The parameters A_n, a_n, and U_{tn} are functions of θ interpolated with the values in Table 2; therefore, σ_{0VHtn} is also a function of θ. In practice, the procedure of wind inversion using H14 is:

Step 1: Determine the WSG based on comparing σ_{0VH} with σ_{0VHt1}, σ_{0VHt2}, and σ_{0VHt3}, that is, $n=1$ for $\sigma_{0VH}<\sigma_{0VHt1}$, 2 for $\sigma_{0VHt1}\leq\sigma_{0VH}<\sigma_{0VHt2}$, 3 for $\sigma_{0VHt2}\leq\sigma_{0VH}<\sigma_{0VHt3}$, and 4 for $\sigma_{0VH}\geq\sigma_{0VHt3}$.

Step 2: Obtain $A_n(\theta)$ and $a_n(\theta)$ by interpolating the LUT (Table 2).

Step 3: Calculate wind speed using (8).

4. Results of *VH* Simulation and Wind Speed Inversion

In this section, we present results of *VH* simulation and U_{10} inversion using the five GMFs ($H14_S$, $H14_E$, Z14, $vZ13_S$, and $vZ13_E$) and three data sets (BSH, $KNMI_S$, and $KNMI_E$) described in the last two sections. Because the error statistics are distorted by the low-SNR data points, in the following discussions, we exclude the

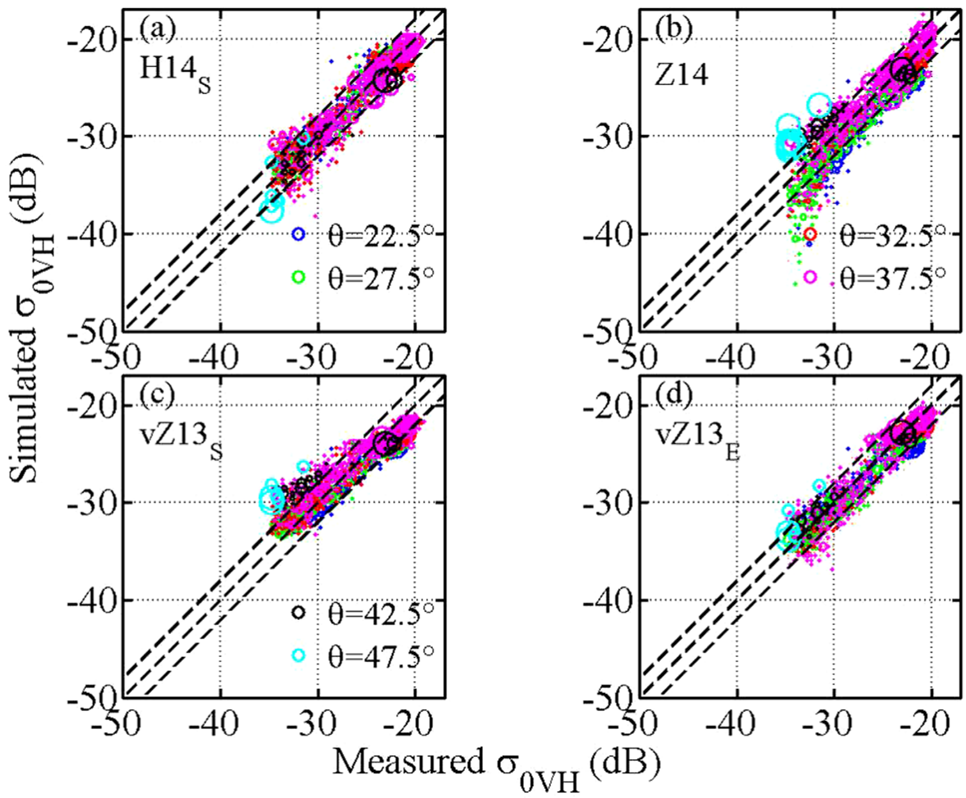

Figure 4. Comparison of simulated and measured *VH* of the BSH data set: (a) $H14_S$, (b) Z14, (c) $vZ13_S$, and (d) $vZ13_E$. The data are sorted in six incidence angle bins and plotted with the same color scheme used in Figures 1 and 2.

cases of measured *VH* less than NESZ+1 in dB. This restriction reduces the useful data by 15%, 2%, and 13%, respectively, for BSH, $KNMI_S$, and $KNMI_E$, mainly in low wind groups (Table 1).

Figure 4 shows the comparison of measured and GMF-simulated *VH* with wind speed and incidence angle as input for the BSH data set. The data are sorted into six θ bins coded in the same color scheme of Figures 1 and 2, and the size of the plotted symbol is proportional to the data density within the same θ bin. The 1:1 diagonal line and ± 2 dB envelops are shown with dashed lines. The data scatter is larger in the low wind region with lower SNR. Overall, $H14_S$ and $vZ13_E$ simulations are in better agreement with the field data compared to Z14 and $vZ13_S$.

Figure 5a shows the probability density function (pdf) of the *VH* difference (simulated minus measured) in dB $\delta\sigma_{0VH}^{dB}(\theta)$, and Figure 5b plots $\delta\sigma_{0VH}^{dB}(\theta)$ versus $\sigma_{0VH}^{dB}(\theta)$. The difference is generally smaller and more narrowly distributed near 0 dB in the $H14_S$ and $vZ13_E$ results. The percentage of difference for ($H14_S$, Z14, $vZ13_S$, and $vZ13_E$) is (88, 77, 81, and 89) within 2 dB and (68, 50, 52, and 64) within 1 dB. The largest difference is generally in the data portion with low SNR (Figure 5b).

Table 3 lists more detailed statistics of mean and root mean squares (RMS) *VH* difference in six θ bins and three wind speed ranges. In general, the RMS values are somewhat better in GMFs with θ sorting ($H14_S$ and $vZ13_E$ in low-to-strong winds). The mean difference (bias) has an obvious monotonic trend with θ for Z14 and $vZ13_S$, which do not include the θ factor.

Figure 6 shows the result of wind speed inversion of the BSH data set using four GMFs ($H14_S$, Z14, $vZ13_S$, and $vZ13_E$). The pdf of the wind speed difference δU_{10} (inverted minus measured) is displayed in Figure 6a and the scatterplot of inverted versus measured U_{10} is shown in Figure 6b with the color scheme identical to that used in Figure 6a. The better performance of the H14 algorithm is manifested in the narrower distribution of δU_{10} near 0 m/s (Figure 6a) and more compact cluttering of data about the 1:1 diagonal line (Figure 6b). The percentage of velocity difference for ($H14_S$, Z14, $vZ13_S$, and $vZ13_E$) is (95, 95, 70, and 90) within 5 m/s, and (81, 78, 52, and 74) within 3 m/s. Table 4 lists more detailed statistics of mean and RMS difference

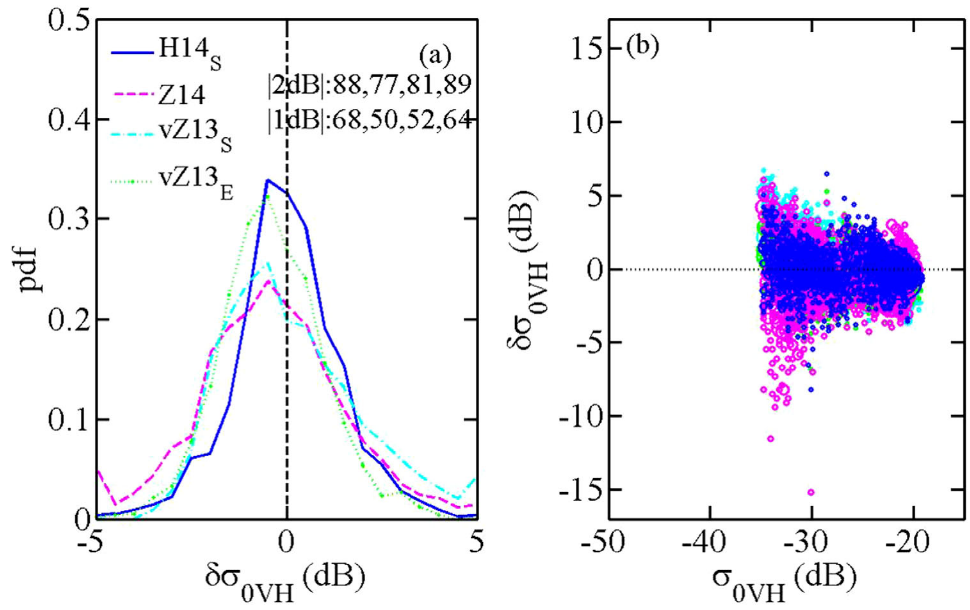

Figure 5. The *VH* simulation using four different GMFs ($H14_S$, Z14, $vZ13_S$, and $vZ13_E$): (a) the pdf of $\delta\sigma_{0VH}^{dB}$ and (b) the scatterplot of $\delta\sigma_{0VH}^{dB}$ versus σ_{0VH}^{dB}. The size of the plotting symbol is proportional to the number of data points at the plotting coordinates; BSH data set.

between inverted and measured U_{10} in six θ bins and three wind speed ranges. Consistent with, and similar to the comparison of simulated and measured *VH*, a monotonic θ dependence in the mean difference (bias) is found in Z14 and $vZ13_S$, and the $H14_S$ GMF produces better difference statistics overall.

The comparison results of *VH* simulation and wind speed inversion using four GMFs ($H14_S$, Z14, $vZ13_S$, and $vZ13_E$) for the $KNMI_S$ data set are summarized in Figure 7 (showing the scatterplots of *VH*) and Figure 8 (showing the pdfs of $\delta\sigma_{0VH}$ and δU_{10}). The percentage of the simulated and measured *VH* difference for ($H14_S$, Z14, $vZ13_S$, and $vZ13_E$) is (77, 66, 78, and 77) within 2 dB, and (52, 43, 50, and 53) within 1 dB (Figure

Table 3. Mean and Standard Deviation of δVH

	BSH				$KNMI_S$				$KNMI_E$			
Sorted	($H14_S$)	(Z14)	(vZ13s)	(vZ13E)	($H14_S$)	(Z14)	(vZ13s)	(vZ13E)	($H14_E$)	(Z14)	(vZ13s)	($vZ13_E$)
RMS Difference												
All data:	9.61E-04	1.21E-03	1.25E-03	9.40E-04	2.28E-03	4.35E-03	1.88E-03	2.05E-03	7.45E-04	9.67E-04	1.01E-03	8.15E-04
θ 20–25	9.24E-04	1.01E-03	1.16E-03	9.38E-04	1.60E-03	1.60E-03	1.47E-03	1.48E-03	7.31E-04	8.38E-04	8.64E-04	7.86E-04
θ 25–30	8.92E-04	8.16E-04	1.06E-03	7.81E-04	2.14E-03	1.64E-03	1.45E-03	1.39E-03	8.54E-04	1.04E-03	1.12E-03	9.60E-04
θ 30–35	1.05E-03	1.18E-03	1.34E-03	1.00E-03	1.78E-03	3.00E-03	1.77E-03	1.69E-03	7.06E-04	8.63E-04	1.07E-03	7.72E-04
θ 35–40	9.58E-04	1.40E-03	1.29E-03	1.05E-03	2.13E-03	3.47E-03	1.63E-03	1.80E-03	7.38E-04	8.12E-04	1.04E-03	7.69E-04
θ 40–45	7.29E-04	7.22E-04	1.05E-03	4.36E-04	3.18E-03	7.35E-03	2.26E-03	2.56E-03	7.49E-04	9.41E-04	9.17E-04	7.62E-04
θ 45–50	1.66E-04	3.32E-04	3.73E-04	2.45E-04	1.78E-03	2.87E-03	1.51E-03	1.94E-03	6.67E-04	6.88E-04	5.75E-04	7.17E-04
$U10 < 15$	3.21E-04	4.25E-04	4.14E-04	3.20E-04	7.27E-04	8.12E-04	7.99E-04	7.52E-04	4.71E-04	5.78E-04	5.73E-04	4.57E-04
$U10$ 15–30	1.30E-03	1.29E-03	1.42E-03	1.23E-03	1.94E-03	2.03E-03	1.78E-03	1.85E-03	9.76E-04	1.21E-03	1.31E-03	1.10E-03
$U10 \geq 30$	1.19E-03	1.88E-03	1.37E-03	1.39E-03	3.11E-03	6.47E-03	2.41E-03	2.62E-03	9.29E-04	1.46E-03	1.10E-03	1.10E-03
Bias												
All data:	−1.01E-05	−1.49E-04	−4.65E-04	−2.92E-04	6.48E-04	1.68E-03	−2.40E-04	4.53E-04	−1.04E-05	−1.19E-04	5.72E-05	−1.94E-04
θ 20–25	1.20E-04	−8.11E-04	−6.84E-04	−4.47E-04	6.74E-04	−9.02E-04	−1.04E-03	−5.45E-04	−9.93E-05	−7.41E-04	−4.31E-04	−3.95E-04
θ 25–30	1.83E-04	−5.25E-04	−4.92E-04	−3.56E-04	1.77E-03	5.53E-04	−4.95E-04	2.03E-04	1.05E-04	−4.76E-04	−1.69E-04	−3.40E-04
θ 30–35	−8.44E-05	−8.50E-05	−7.00E-04	−3.99E-04	3.23E-04	1.06E-03	−7.48E-04	−1.16E-04	−1.31E-05	−2.05E-04	4.67E-05	−2.37E-04
θ 35–40	2.01E-05	5.02E-04	−2.01E-04	−4.86E-05	3.50E-04	1.49E-03	−4.42E-04	1.54E-04	−3.00E-05	7.64E-05	2.04E-04	−1.08E-04
θ 40–45	−4.61E-04	1.30E-04	1.47E-04	−6.76E-05	7.25E-04	4.10E-03	3.62E-04	1.27E-03	−1.32E-05	1.93E-04	1.65E-04	−2.05E-04
θ 45–50	−5.73E-05	6.56E-04	9.25E-04	2.48E-04	2.92E-04	3.14E-03	1.38E-03	2.20E-03	1.99E-05	5.50E-04	6.24E-04	1.70E-04
$U10 < 15$	−2.98E-05	−8.63E-05	2.00E-04	−1.29E-04	−1.45E-04	−9.95E-05	1.76E-04	−2.53E-04	−1.36E-06	5.66E-06	2.75E-04	−1.31E-04
$U10$ 15–30	−2.62E-05	−5.00E-04	−9.77E-04	−4.27E-04	3.94E-04	3.66E-04	−3.42E-04	2.57E-04	−3.74E-05	−3.31E-04	−1.84E-04	−2.74E-04
$U10 \geq 30$	3.05E-04	2.41E-03	−1.88E-03	−5.44E-04	1.67E-03	5.93E-03	−1.72E-04	1.30E-03	7.12E-04	2.39E-03	−1.42E-03	−1.36E-04

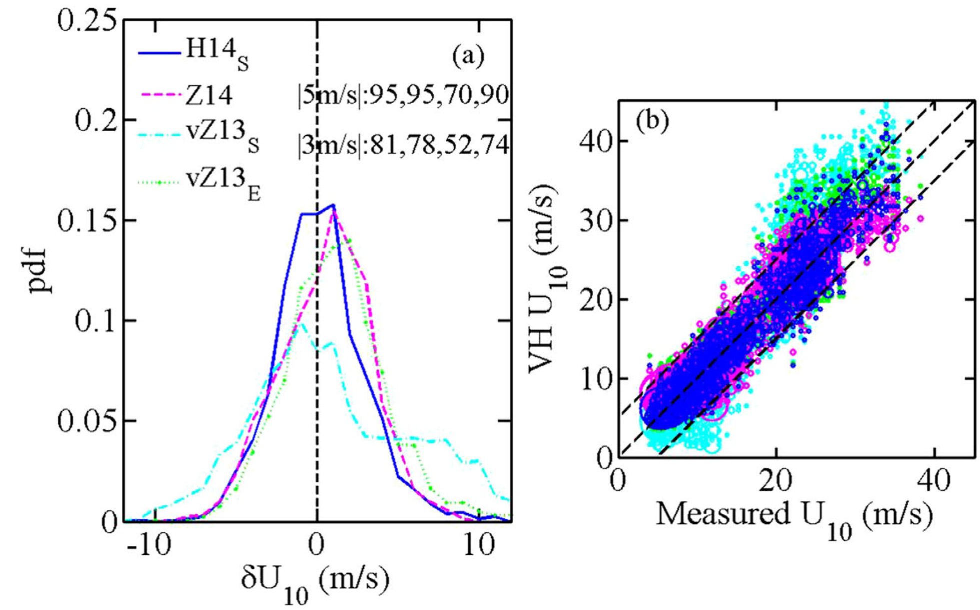

Figure 6. The wind speed inversion using four different GMFs (H14$_S$, Z14, vZ13$_S$, and vZ13$_E$): (a) the pdf of δU_{10} and (b) the scatterplot of measured and inverted U_{10}; the size of the plotting symbol is proportional to the number of data points at the plotting coordinates; BSH data set.

8a). The percentage of the inverted and measured U_{10} difference for (H14$_S$, Z14, vZ13$_S$, and vZ13$_E$) is (75, 69, 57, and 69) within 5 m/s, and (53, 52, 36, and 49) within 3 m/s (Figure 8b).

Similarly, the comparison results for the KNMI$_E$ data set are summarized in Figures 9 and 10 in the same format as that for the KNMI$_S$ data set. The percentage of the simulated and measured *VH* difference for (H14$_E$, Z14, vZ13$_S$, and vZ13$_E$) is (85, 74, 70, and 86) within 2 dB, and (62, 48, 46, and 62) within 1 dB (Figure 10a). The percentage of the inverted and measured U_{10} difference for (H14$_E$, Z14, vZ13$_S$, and vZ13$_E$) is (97, 91, 75, and 94) within 5 m/s, and (87, 72, 55, and 84) within 3 m/s (Figure 10b).

Table 4. Mean and Standard Deviation of $\delta U10$

	BSH				KNMI$_S$				KNMI$_E$			
Sorted	(H14$_S$)	(Z14)	(vZ13s)	(vZ13E)	(H14$_S$)	(Z14)	(vZ13s)	(vZ13e)	(H14$_E$)	(Z14)	(vZ13s)	(vZ13$_E$)
RMS Difference												
All data	2.77	2.82	5.13	3.11	4.95	5.32	6.82	5.44	2.45	3.25	4.76	2.79
θ 20–25	2.64	2.25	4.75	3.33	4.68	3.57	5.93	5.00	2.22	2.35	3.85	2.93
θ 25–30	2.13	1.95	4.40	2.63	3.74	3.23	5.12	4.35	2.52	2.62	4.75	3.27
θ 30–35	3.04	2.46	4.99	3.24	4.68	4.12	5.92	4.45	2.61	2.76	4.73	2.80
θ 35–40	2.93	2.75	4.88	3.16	5.07	5.44	6.29	5.29	2.62	3.00	4.78	2.68
θ 40–45	2.32	2.53	5.61	2.05	5.66	5.58	6.81	5.86	2.34	2.50	4.57	2.30
θ 45–50	2.41	1.49	1.11	1.22	4.69	5.21	7.31	4.72	2.10	2.26	3.34	2.28
$U10 < 15$	1.98	2.44	2.98	2.09	3.65	4.09	4.55	3.51	2.33	3.19	3.59	2.26
$U10$ 15–30	3.29	2.96	5.26	3.82	4.65	4.84	7.27	5.24	2.58	3.28	5.23	3.32
$U10 \geq 30$	3.56	2.22	3.36	3.42	5.67	4.71	6.27	5.98	2.26	1.91	2.99	3.06
Bias												
All data	0.19	0.53	1.17	1.15	−0.95	−2.01	0.61	−1.12	−0.32	0.50	−0.80	0.47
θ 20–25	−0.09	2.53	2.80	1.77	−0.42	2.26	4.40	1.77	0.17	3.18	1.95	1.26
θ 25–30	−0.48	1.71	1.68	1.49	−3.23	−0.60	1.49	−0.68	−0.90	2.11	0.49	0.80
θ 30–35	0.44	0.42	1.90	1.52	−0.55	−1.19	2.01	0.26	−0.58	0.64	−0.49	0.53
θ 35–40	0.09	−1.02	−0.11	0.29	−0.38	−1.42	1.57	−0.33	−0.41	−0.73	−1.67	0.12
θ 40–45	1.29	−1.57	−2.25	0.08	−0.93	−4.65	−1.29	−3.09	−0.25	−0.32	−1.70	0.50
θ 45–50	1.81	−4.23	−8.85	−2.25	−0.44	−6.56	−6.12	−5.77	0.00	−2.57	−3.94	−0.52
$U10 < 15$	0.00	0.53	−1.89	0.88	0.26	0.49	−1.64	0.89	−0.48	0.26	−2.45	0.29
$U10$ 15–30	0.39	0.93	3.83	1.42	−0.42	−0.85	1.17	−0.62	−0.09	0.87	1.16	0.71
$U10 \geq 30$	0.12	−2.95	4.88	1.16	−2.90	−6.21	0.24	−3.37	−1.70	−3.04	3.92	0.15

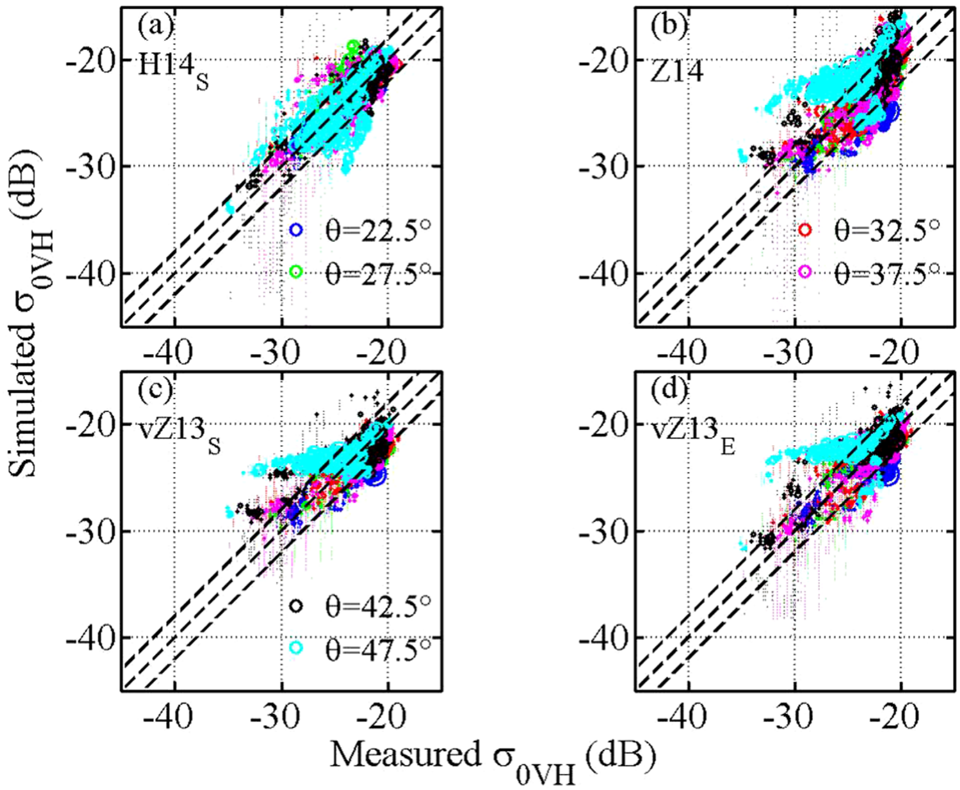

Figure 7. Same as Figure 4 but for the $KNMI_S$ data set.

More detailed statistics of mean and RMS difference of $\delta\sigma_{0VH}$ and δU_{10} in six θ bins and three wind speed ranges for $KNMI_S$ and $KNMI_E$ are also listed in Tables 3 and 4. For all three data sets, the *VH* simulation and U_{10} inversion using the GMFs that consider θ dependence produce less biases and smaller RMS differences in general.

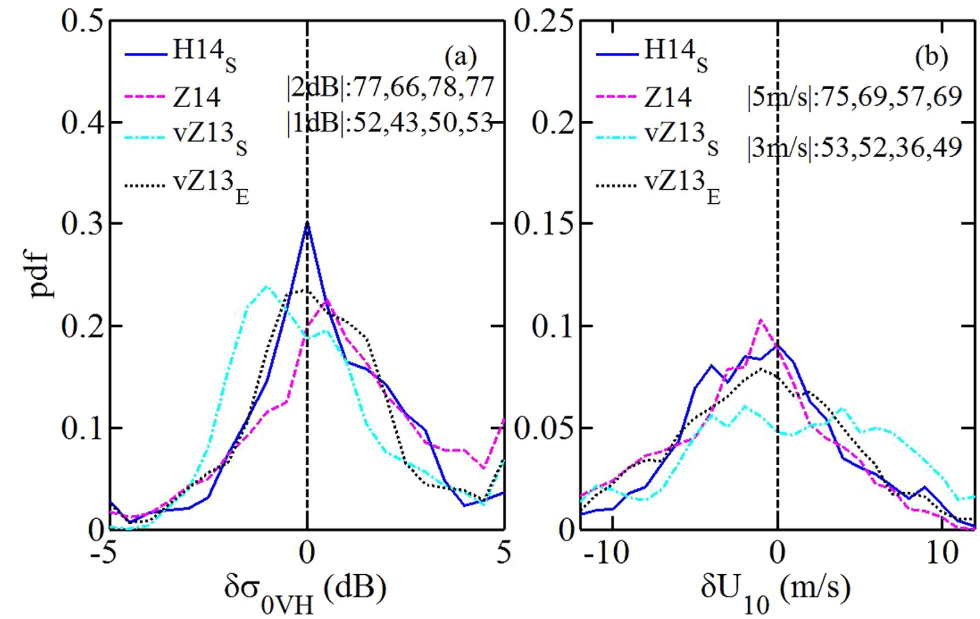

Figure 8. The pdf of (a) $\delta\sigma_{0VH}^{dB}$ and (b) δU_{10} for the $KNMI_S$ data set.

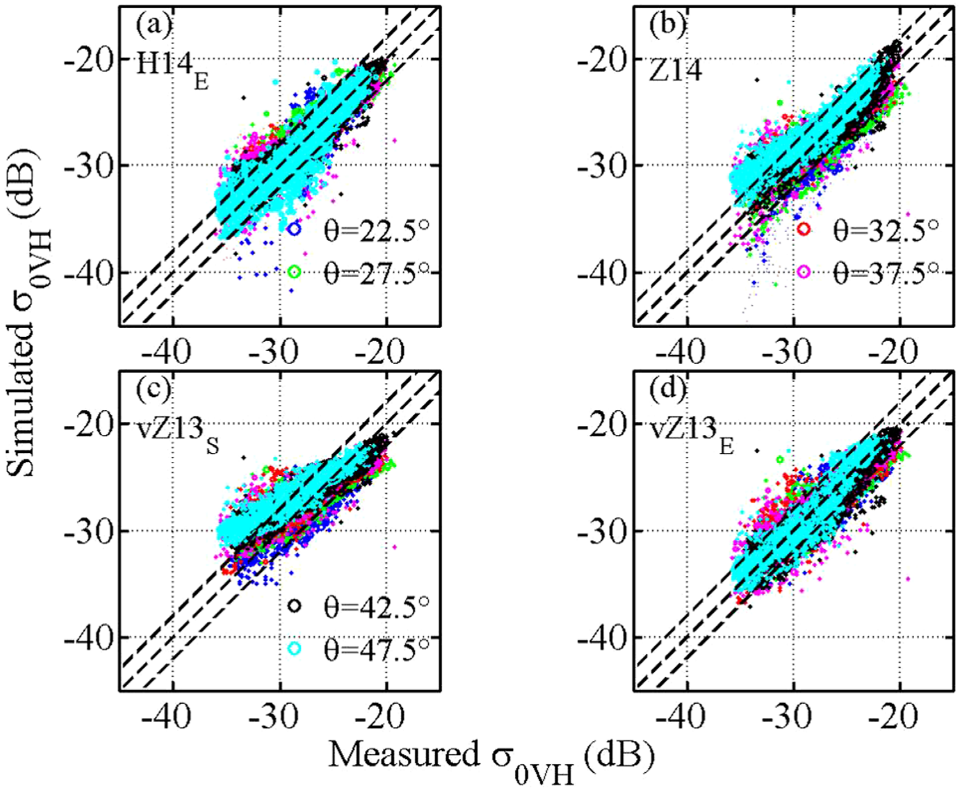

Figure 9. Same as Figure 4 but for the KNMI$_E$ data set.

5. Discussion

5.1. Noise Treatment

The KNMI$_S$ and KNMI$_E$ data sets are collected for 13 and 19 hurricane scenes respectively, and the coverage of low wind cases is relatively sparse. As a result, the lowest wind speed group of the BSH data set (Figures 1 and 2)

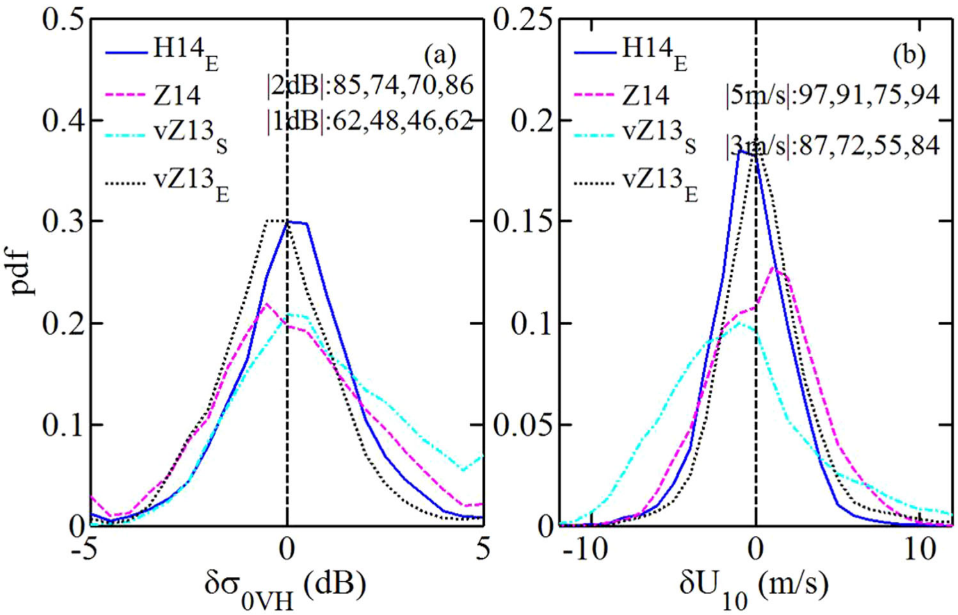

Figure 10. The pdf of (a) $\delta\sigma_{0VH}^{dB}$ and (b) δU_{10} for the KNMI$_E$ data set.

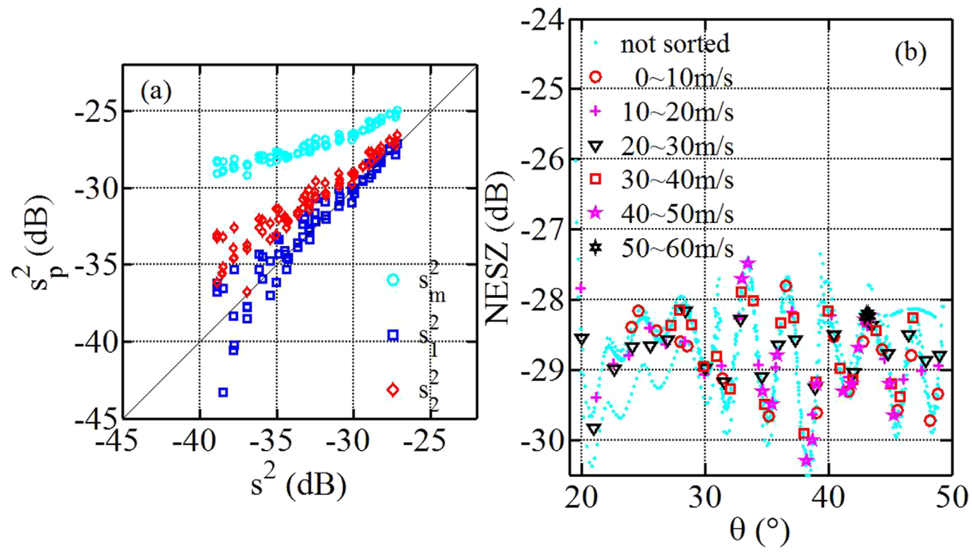

Figure 11. (a) Simulation example of data processing to recover weak signal by subtracting the mean noise in measurements without the noise information. (b) The NESZ of $KNMI_S$ data set.

is used to establish the $A_1(\theta_i)$ coefficients of the power law function in WSG1. These $A_1(\theta_i)$ are then used to establish the $A_n(\theta_i)$ in the nth WSG ($n > 1$) from the matching equation (2). Unfortunately, the BSH data set does not include the noise data. Because *VH* in WSG1 is typically of lower SNR, the noise treatment is especially critical to obtain the correct power law relationship for $\sigma_{0VH}(U_{10}|\theta)$.

In the absence of noise information in low-SNR measurements, we attempt recovering the average weak signal by subtracting the nominal mean noise during data processing. Figure 11a shows a simulation example of weak signals of variance s^2 (between -39 and -27 dB level) with noise of comparable variance n^2 distributed randomly between 0 and $2 \times 10^{-2.9}$; thus, the mean noise is -29 dB. The measured signal with noise averaged over 50 realizations is represented by s_m^2. The recovered signal from data processing ($s_p^2 = s_m^2 - n^2$) by subtracting the mean noise of -29 dB, shown as s_1^2, resembles the original signal well. However, if the mean noise is not specified correctly, the fidelity of signal recovery may suffer, as illustrated by the result s_2^2 assuming a mean noise of -30 dB.

Without noise information, -30 dB was used for noise subtraction in a previous analysis of the BSH data set [*Hwang et al*., 2014]. However, -30 dB is the nominal noise floor rather than the mean noise [*Hwang et al*., 2010a]. Both KNMI data sets ($KNMI_S$ and $KNMI_E$) have extracted the noise data (NESZ) of the radar scattering measurements. Figure 11b shows the NESZ dependence on incidence angle and wind speed. The complicated variations are mainly caused by the merging together of several different radar beams to form the wide swath coverage of the R2 ScanSAR mode. The mean noise is about -29 dB, which is used in the data processing of BSH data set in this study.

Figure 12 shows the considerable difference of the results in the low wind speed region of the BSH data set processed with -29 and -30 dB mean noise (Figures 12a and 12c, respectively). The result processed with -29 dB mean noise appears to be in better agreement with the $KNMI_S$ data set (Figure 12b). For reference, identical line segments with various wind speed exponents are plotted in the three plots of Figure 12.

5.2. Wind Speed Range and Wave Breaking Detection

Although cross-pol or depolarization of sea returns has been reported since the 1960s [e.g., *Valenzuela*, 1967], its potential utility has not generated much interest because of its weak magnitude. This situation is changing with our increased appreciation of the advantage of the *VH* signal (probable nonsaturation, increased sensitivity toward high winds, improving directional resolution of VV wind retrieval, improving coastal wind retrieval, and higher breaking contribution) as described in section 1. With careful noise treatment during data processing, the range of wind speeds retrievable using the *VH* signal includes mild and moderate conditions (Figure 6 and Table 4).

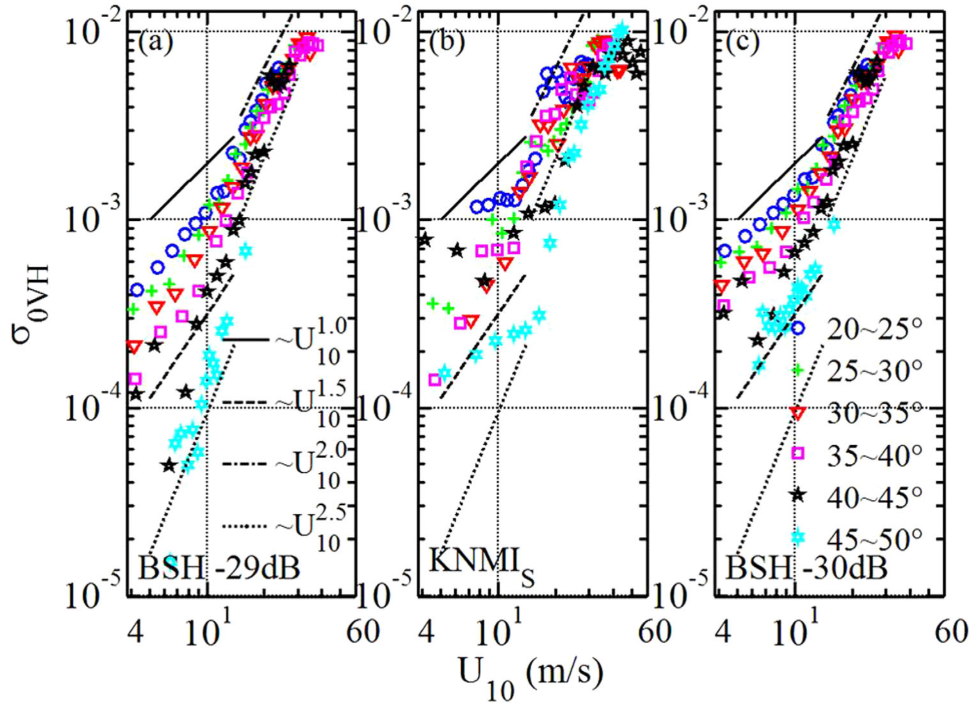

Figure 12. Noise processing of BSH data set using mean noise of (a) −29 dB and (c) −30 dB. The $KNMI_S$ data set is shown in (b) for comparison. Identical line segments with various wind speed exponents are plotted in each figure for reference.

The pursuit of *VH* wind retrieval capability for a broader wind speed range is of interest in regard to breaking wave investigations. Microwave polarimetry has been exploited for breaking wave analysis; for example, the *VV/HH* polarization ratio and *HH* Doppler spectrum analysis of sea spikes have produced interesting results quantifying the breaking length and velocity scales [e.g., *Frasier et al.*, 1998; *Hwang et al.*, 2008a, 2008b]. The breaking contribution seems to be even stronger for the *VH* sea returns compared to *HH* [e.g., *Hwang et al.*, 2010a, 2010b; *Voronovich and Zavorotny*, 2011, 2014]. The potential for extracting surface wave breaking information from *VH* is worth exploring.

5.3. Other Factors Affecting Backscattering

The cross-pol GMF as presented in this paper considers wind speed as the only cause of backscattering variations. Microwave backscattering from the ocean surface is in fact quite complicated. In essence, any factor that modifies the ocean surface roughness will also modify the microwave backscattering. In addition to the rain factor discussed in section 1, many variables impacting air-sea momentum flux also impact the ocean surface roughness that causes microwave scattering. Examples include the air-sea boundary layer stability condition, sea state and the complex issues of mixed sea conditions (e.g., directions between wind, sea and swell; peak periods and significant wave heights of wind sea and swell components), as well as surfactants. Furthermore, scattering measurements are inherently stochastic; the variation of a couple of decibels at a given incidence angle and wind speed is not uncommon. Extensive discussions on the scatterometer data interpretation have been published [e.g., *Stoffelen and Anderson*, 1997a, 1997b].

6. Summary

In this paper, we present a framework to construct the C-band *VH* GMF. The method is built upon the piecewise power law relationship between $\sigma_{0VH}(\theta)$ and U_{10}. This is consistent with the property of piecewise power law relationship of the short-scale wind-generated waves that serve as the Bragg resonance roughness elements of microwave scattering from the ocean surface [e.g., *Hwang and Wang*, 2004; *Hwang et al.*, 2013].

Recognizing the difficulty of assembling sufficient collocated and simultaneous radar scattering and wind velocity measurements to cover a broad range of wind speeds and incidence angles, the method is designed to work with a partial knowledge of the power law function relating $\sigma_{0VH}(\theta)$ and U_{10}. In particular, the primary required input parameters are the exponents of the power law functions in various θ bins and WSGs, and the proportionality coefficient for the lowest WSG, of which the most abundant data are expected. It is also designed for easy refinement as new data become available or when data sets with different characteristics require special GMF variations.

Examples of *VH* simulation and wind speed inversion using several different GMFs (H14$_S$, H14$_E$, Z14, vZ13$_S$, and vZ13$_E$) are presented in section 4. The comparison with three data sets (BSH, KNMI$_S$, and KNMI$_E$) illustrates that the GMFs including explicit θ dependence perform better in the statistics (bias and RMS difference) of *VH* simulation and wind speed inversion. The θ dependence in the proposed GMFs extends to the full range of wind speeds in the available data sets.

With careful noise treatment, the *VH* wind retrieval is not limited to strong or severe conditions (Figure 6 and Table 4). In addition to wind retrieval, the *VH* signal contains larger contributions from wave breaking in comparison to copol sea returns. Extracting wave breaking information using the *VH* is also a feasible application.

Acknowledgments
This work is supported by the Office of Naval Research ("Breaking-wave effects under high winds" and "Oceanic whitecaps as a surface expression of under and above water processes: Toward an integral remote sensing of the air-sea interface"). We thank the Canadian Space Agency (CSA) for providing RADARSAT-2 imagery, NOAA HRD for supplying SFMR and H*Wind, NDBC for buoy observations, ECMWF for numerical forecast winds, and the EUMETSAT Ocean and the Sea Ice Satellite Application Facility, which supports the KNMI work and generated collocated data sets. We also acknowledge the support of the Canadian Space Agency (GRIP Program), Chinese National High Technology Research and Development (863) Program (grant 2013AA09A505), and the National Science Youth Foundation of Jiangsu (grant BK2012467). The three data sets used in the analysis of this paper were assembled by Biao Zhang (zhangbiao@nuist.edu.cn, BSH data set) and Gerd-Jan van Zadelhoff (zadelhof@knmi.nl, KNMI$_S$ and KNMI$_E$ data sets). RADARSAT-2 data distribution requires explicit permission from CSA. The NRL publication number is NRL/JA/7260-14-0213.

References

Belmonte Rivas, M., A. Stoffelen, and G.-J. van Zadelhoff (2014), The benefit of HH and VH polarization in retrieving extreme wind speeds for an ASCAT-type scatterometer, *IEEE Trans. Geosci. Remote Sens.*, *52*, 4273–4280.

DiNapoli, S. M., M. Bourassa, and M. D. Powell (2012), Uncertainty and intercalibration analysis of H*Wind, *J. Atmos. Oceanic Technol.*, *29*, 822–833.

Fois, F., P. Hoogeboom, F. Le Chevalier, and A. Stoffelen (2014), Future ocean scatterometry at very strong winds, paper presented at IEEE Proceedings of International Geoscience and Remote Sensing Symposium, IEEE, Quebec, Canada.

Frasier, S. J., Y. Liu, and R. E. McIntosh (1998), Space-time properties of radar sea spikes and their relation to wind and wave conditions, *J. Geophys. Res.*, *103*, 18,745–18,757.

Hersbach, H. (2003), CMOD5—An improved geophysical model function for ERS C-band scatterometry, *ECMWF Tech. Memo. 395*, 52 pp., Eur. Cent. for Medium-Range Weather Forecasts, Reading, U. K.

Horstmann, J., C. Wackerman, S. Falchetti, and S. Maresca (2013), Tropical cyclone winds retrieved from synthetic aperture radar, *Oceanography*, *26*, 46–57.

Hwang, P. A., and D. W. Wang (2004), An empirical investigation of source term balance of small scale surface waves, *Geophys. Res. Lett.*, *31*, L15301, doi:10.1029/2004GL020080.

Hwang, P. A., M. A. Sletten, and J. V. Toporkov (2008a), Analysis of radar sea return for breaking wave investigation, *J. Geophys. Res.*, *113*, C02003, doi:10.1029/2007JC004319.

Hwang, P. A., M. A. Sletten, and J. V. Toporkov (2008b), Breaking wave contribution to low grazing angle radar backscatter from the ocean surface, *J. Geophys. Res.*, *113*, C09017, doi:10.1029/2008JC004752.

Hwang, P. A., B. Zhang, and W. Perrie (2010a), Depolarized radar return for breaking wave measurement and hurricane wind retrieval, *Geophys. Res. Lett.*, *37*, L01604, doi:10.1029/2009GL041780.

Hwang, P. A., B. Zhang, J. V. Toporkov, and W. Perrie (2010b), Comparison of composite Bragg theory and quad-polarization radar backscatter from RADARSAT-2: With applications to wave breaking and high wind retrieval, *J. Geophys. Res.*, *115*, C08019, doi:10.1029/2009JC005995.

Hwang, P. A., D. M. Burrage, D. W. Wang, and J. C. Wesson (2013), Ocean surface roughness spectrum in high wind condition for microwave backscatter and emission computations, *J. Atmos. Oceanic Technol.*, *30*, 2168–2188, doi:10.1175/JTECH-D-12-00239.1.

Hwang, P. A., W. Perrie, and B. Zhang (2014), Cross polarization radar backscattering from the ocean surface and its dependence on wind velocity, *IEEE Geosci. Remote Sens. Lett.*, *21*, 2188–2192, doi:10.1109/LGRS.2014.2324276.

Klotz, B. W., and E. W. Uhlhorn (2012), Improving SFMR surface wind measurements in heavy rain conditions, paper presented at AMS 2012 (7C.6), 92nd Annual Meeting, Am. Meteorol. Soc., New Orleans, La.

Lin, C.-C., M. Betto, M. B. Rivas, A. Stoffelen, and J. de Kloe (2012), EPS-SG wind scatterometer concept trade-offs and wind retrieval performance assessment, *IEEE Trans. Geosci. Remote Sens.*, *50*, 2458–2472, doi:10.1109/TGRS.2011.2180393.

Slade, R. (2009), RADARSAT-2 product description, *Doc. MDA RN-SP-52-1238*, 46 pp., MacDonald, Dettwiler and Associates Ltd., Richmone, B.C., Canada.

Stoffelen, A. (1998), Towards the true surface wind speed: Error modeling and calibration using triple collocation, *J. Geophys. Res.*, *103*, 7755–7766.

Stoffelen, A., and D. Anderson (1997a), Scatterometer data interpretation: Measurement space and inversion, *J. Atmos. Oceanic Technol.*, *14*, 1298–1313.

Stoffelen, A., and D. Anderson (1997b), Scatterometer data interpretation: Derivation of the transfer function, CMOD4, *J. Geophys. Res.*, *102*, 5767–5780.

Vachon, P. W., and J. Wolfe (2011), C-band cross-polarization wind speed retrieval, *IEEE Geosci. Remote Sens. Lett.*, *8*, 456–458.

Valenzuela, G. R. (1967), Depolarization of EM waves by slightly rough surfaces, *IEEE Trans. Antennas Propag.*, *15*, 552–557.

van Zadelhoff, G.-J., A. Stoffelen, P. W. Vachon, J. Wolfe, J. Horstmann, and M. Belmonte Rivas (2013), Scatterometer hurricane wind speed retrievals using cross polarization, *Atmos. Meas. Tech. Discuss.*, *6*, 7945–7984.

van Zadelhoff, G.-J., A. Stoffelen, P. W. Vachon, J. Wolfe, J. Horstmann, and M. Belmonte Rivas (2014), Retrieving hurricane wind speeds using cross polarization C-band measurements, *Atmos. Meas. Tech.*, *7*, 437–449.

Verhoef, A., and A. Stoffelen (2013), ASCAT Wind Product User Manual Version 1.13, Document external project: 2013, *Doc. SAF/OSI/CDOP/KNMI/TEC/MA/126*, EUMETSAT, Royal Netherlands, Meteorological Institute, De Bilt, Netherlands.

Voronovich, A. G., and V. U. Zavorotny (2011), Depolarization of microwave backscattering from a rough sea surface: Modeling with small-slope approximation, in *International Geoscience and Remote Sensing Symposium*, pp. 2003–2036, IEEE, Vancouver, Canada.

Voronovich, A. G., and V. U. Zavorotny (2014), Full-polarization modeling of monostatic and bistatic radar scattering from a rough sea surface, *IEEE Trans. Antennas Propag.*, *62*, 1363–1371.

Yueh, S., S. Dinardo, A. Fore, and F. Li (2010), Passive and active L-band microwave observations and modeling of ocean surface winds, *IEEE Trans. Geosci. Remote Sens.*, *48*, 3087–3100.

Yueh, S. H., W. J. Wilson, and S. Dinardo (2002), Polarimetric radar remote sensing of ocean surface wind, *IEEE Trans. Geosci. Remote Sens.*, *40*, 793–800.

Zhang, B., and W. Perrie (2012), Cross-polarized synthetic aperture radar: A new potential technique for hurricanes, *Bull. Am. Meteorol. Soc.*, *93*, 531–541, doi:10.1175/BAMS-D-11-00001.1.

Zhang, B., W. Perrie, and Y. He (2011), Wind speed retrieval from RADARSAT-2 quad-polarization images using a new polarization ratio model, *J. Geophys. Res.*, *116*, C08008, doi:10.1029/2010JC006522.

Zhang, B., W. Perrie, P. W. Vachon, X. Li, W. G. Pichel, J. Guo, and Y. He (2012), Ocean vector winds retrieval from C-band fully polarimetric SAR measurements, *IEEE Trans. Geosci. Remote Sens.*, *50*, 4252–4261.

Zhang, B., W. Perrie, P. Vachon, J. A. Zhang, E. W. Uhlhorn, and Y. He (2014), High resolution hurricane vector winds from C-band dual-polarization SAR observations, *J. Atmos. Oceanic Technol.*, *31*, 272–286.